

RESEARCH ARTICLE

Open Access



Hydropathicity-based prediction of pain-causing NaV1.7 variants

Makros N. Xenakis^{1,2*}, Dimos Kapetis³, Yang Yang^{4,5}, Monique M. Gerrits⁶, Jordi Heijman⁷, Stephen G. Waxman^{8,9}, Giuseppe Lauria^{3,10}, Catharina G. Faber¹¹, Ronald L. Westra¹², Patrick J. Lindsey^{1,13} and Hubert J. Smeets^{1,2}

*Correspondence:

mrksxenakis@gmail.com

¹ Department

of Toxicogenomics, Section
Clinical Genomics, Maastricht
University, PO Box 616,
6200 MD Maastricht, The
Netherlands

Full list of author information
is available at the end of the
article

Abstract

Background: Mutation-induced variations in the functional architecture of the NaV1.7 channel protein are causally related to a broad spectrum of human pain disorders. Predicting in silico the phenotype of NaV1.7 variant is of major clinical importance; it can aid in reducing costs of in vitro pathophysiological characterization of NaV1.7 variants, as well as, in the design of drug agents for counteracting pain-disease symptoms.

Results: In this work, we utilize spatial complexity of hydropathic effects toward predicting which NaV1.7 variants cause pain (and which are neutral) based on the location of corresponding mutation sites within the NaV1.7 structure. For that, we analyze topological and scaling hydropathic characteristics of the atomic environment around NaV1.7's pore and probe their spatial correlation with mutation sites. We show that pain-related mutation sites occupy structural locations in proximity to a hydrophobic patch lining the pore while clustering at a critical hydropathic-interactions distance from the selectivity filter (SF). Taken together, these observations can differentiate pain-related NaV1.7 variants from neutral ones, i.e., NaV1.7 variants not causing pain disease, with 80.5% sensitivity and 93.7% specificity [area under the receiver operating characteristics curve = 0.872].

Conclusions: Our findings suggest that maintaining hydrophobic NaV1.7 interior intact, as well as, a finely-tuned (dictated by hydropathic interactions) distance from the SF might be necessary molecular conditions for physiological NaV1.7 functioning. The main advantage for using the presented predictive scheme is its negligible computational cost, as well as, hydropathicity-based biophysical rationalization.

Keywords: NaV1.7, Missense mutations, Pain, Atomic hydropathicity, Computational modeling, Cumulative hydropathic topology, Scaling, Pathogenicity prediction

Introduction

Voltage-gated sodium channels (NaVChs) are pore-forming proteins embedded in cell membranes. They are members of the ion channels superfamily and their main physiological role is to control transport of sodium ions into the cell. The human NaV1.7 channel is encoded by the *SCN9A* gene and is preferentially expressed in peripheral neurons (e.g., dorsal root ganglion (DRG) nociceptors) responsible for networking pain



© The Author(s), 2021. **Open Access** This article is licensed under a Creative Commons Attribution 4.0 International License, which permits use, sharing, adaptation, distribution and reproduction in any medium or format, as long as you give appropriate credit to the original author(s) and the source, provide a link to the Creative Commons licence, and indicate if changes were made. The images or other third party material in this article are included in the article's Creative Commons licence, unless indicated otherwise in a credit line to the material. If material is not included in the article's Creative Commons licence and your intended use is not permitted by statutory regulation or exceeds the permitted use, you will need to obtain permission directly from the copyright holder. To view a copy of this licence, visit <http://creativecommons.org/licenses/by/4.0/>. The Creative Commons Public Domain Dedication waiver (<http://creativecommons.org/publicdomain/zero/1.0/>) applies to the data made available in this article, unless otherwise stated in a credit line to the data.

signals. The structure of the NaV1.7 α -subunits is that of a pore-forming tetramer via assembly of four heterogeneous domains (DI-DIV). Three intracellular linkers (L1-L3) form structural interconnections among subsequent domains. Each domain comprises six transmembrane helices (S1-S6) organized into a pore module (PM) forming an ion-conduction pathway coupled with a voltage-sensor (VS). Mechanistic description of NaV1.7's function is that VSs react to extracellular changes in ionic concentrations by moving outwards thus exerting a pulling force upon the PM which opens the channel pore. Closed-to-open conformational change leads to channel activation, i.e., renders it conductive to sodium ions. Missense mutations in the *SCN9A* gene can destabilize the NaV1.7's functional architecture thus disrupting physiological sodium-ions current and, consequently, deregulate flow of sodium ions through the pore. At a cellular level, these genetically-caused destabilizations can affect neuronal excitability by inducing a gain-of-function (GOF) effect, i.e., by increasing the net sodium-ions currents, thus triggering a wide spectrum of pain diseases such as inherited erythromelalgia (IEM) [1–30], paroxysmal extreme pain disorder (PEPD) [31–37] and small fiber neuropathy (SFN) [38–42]. A proof of concept for the GOF-pain correlation hypothesis came from identification of missense *SCN9A*-gene mutations inducing a loss-of-function (LOF) effect, i.e., decreasing net sodium-ions current, that is causally related to clinical symptoms of loss of pain sensation [43–45].

Hydrophobic interactions (HIs) represent a summary of fundamental molecular interactions [46] driving molecular phenomena such as protein folding, protein hydrophobic-core stability, self-assembly of amphiphilic molecules, and “dewetting” of molecular surfaces (for a review in HIs-driven phenomena see [47]). Within the field of ion channels research, experimental and computational studies have shown that pore-lining patches of hydrophobic residues are crucial regulators of, both, pore's gating behavior (a phenomenon termed as “hydrophobic gating” [48]) and channel stability [49], e.g., via formation of hydrogen-bonds networks expanding through their surroundings [50, 51]. Crucially, hydrophobic patches (HPs) are widely conserved across voltage-gated channels and often associated with the formation of centrally-located cavity (CC) [52]. Mutations perturbing this hydrophobic motif can lead to drastic changes of net ion currents [53–56].

Computational modeling of HIs combined with biophysical observations extracted from *in vitro* NaVCh pathophysiological characterization can propel our understanding of mechanistic linkages between mutation-induced perturbations and human pain pathophysiology. Key-studies toward this direction were these of Lampert et al [57], and of Yang et al [58] demonstrating how the F1449V mutation, and the in-frame-deletion L955Del, respectively, can disrupt a hydrophobic ring stabilizing the putative activation gate (AG) of the NaV1.7 thus acting as disease-causing molecular triggers. Moreover, computational modeling successfully deduced an energetic coupling between two different IEM-related mutations foreseen by their geometrical proximity in NaV1.7 structure [7]. A question that naturally arose from these studies was whether a detailed examination of HIs network characteristics within a NaV1.7 structure can reveal statistically-significant but also biophysically-relevant differentiations among the WT structure and its variants. This question was probed by Kapetis et al [59]; a network-theoretical computational framework was introduced in order to capture changes in interatomic HIs

within a NaV1.7 structural model induced by pain-related mutations. The study reported on a betweenness centrality network measure achieving a statistically-important differentiation of pain-related variants from a collection of neutrals, i.e., variants not causing pain disease. Notably, this approach highlighted the prominent role that HIs play in NaV1.7's stability and reported on plausible mutation-mechanism scenarios disrupting hydrophobic contacts among neighboring and distant residues. Another remark on the multi-scale nature of HIs was made by the authors of [60] suggesting that a pathogenic mutation in the *KCNA1* gene encoding the human voltage-gated potassium channel KV1.1 can de-tune HIs equilibrium (and, consequently, destabilize KV1.1's pre-open conformation) implying that mutation-induced perturbation effects can destroy finely-tuned network-like HIs expanding throughout the structure as a whole. Interestingly, the fine-tuning hypothesis was proposed also for the NaV1.7; a recent study employing a machine learning (MLE) computational pipeline for predicting NaV1.7's variant pathogenicity suggested that the fine-tuning of the NaV1.7 channel is so delicate that limits classification accuracy of practically any computational approach [61]. Taken together, these observations highlight the highly-cooperative nature of HIs [46] and suggest that even small changes in the hydrophobic spatial distribution profile of a channel structure can have a detrimental impact on the functional architecture which, in turn, might induce clinically-observed alterations of electrophysiology.

Following [59, 61], this study aims at probing the finely-tuned hypothesis for the NaV1.7's atomic hydrophobic environment towards predicting whether a NaV1.7 variant causes pain or not. We demonstrate our approach on a closed-state NaV1.7 structural model (first presented in [7] and later also used in [30, 58]) by investigating cumulative, i.e., scale-dependent, hydrophobic properties of its porous atomic environment in relation to structural locations of missense *SCN9A*-gene mutations. In order to tackle spatial complexities emerging from the highly-cooperative nature of HIs we adopt a modeling approach rooted in the hypothesis that proteins can be represented as self-organized criticality (SOC) [62] archetypes; protein structures are thought to have been evolutionary optimized with respect to extrema in some thermodynamic property (or properties) capturing a qualitative reorganization of the atomic environment [63, 64]. The intra-channel locations where these macroscopic thermodynamic changes take place correspond to so-called critical points of the atomic structure [63, 64]. The highly-cooperative nature of HIs has placed structure-retrieved hydrophobic properties in the epicenter of SOC hypothesis [63–66]). It is important to note that computational evidence for a universal hydrophobic-to-hydrophilic (or inside-outside with “inside” referring to the hydrophobic core, and “outside” referring to the hydrophilic exterior) spatial transition in protein systems was first provided before the formulation of the SOC hypothesis (see [67]). Departing from this phenomenological basis, we here utilize the finite-size scaling analysis methodologies presented in [68, 69] for screening hydrophobic morphology around NaV1.7's pore [68] toward identification of critical points associated with NaV1.7's functional architecture. Biophysical relevance of retrieved observations is justified not only in terms of the scale-invariance of a carefully-chosen cumulative hydrophobicity-property function but also with respect to conserved structural NaV features such as the PM-VSs spatial transition [70, 71] and the architecture of the selectivity filter (SF) [72]. In particular, we demonstrate that the atomic cumulative distribution function

around NaV1.7's pore exhibits a sigmoid profile with inflection points matching closely the conserved PM-VSs spatial transition. This provides a rigorous description of atom-packing geometry and, consequently, a macroscopic partitioning of the atomic environment around the pore allowing for mapping the spatial profile of the atomic cumulative hydrophobicity-property function and mutation sites on two dimensions. The SOC hypothesis is then accepted (or rejected) depending on whether the cumulative hydrophobicity-property function is globally maximized and exhibits power-law-like scaling behavior in the vicinity of the inflection point (or not).

Our mapping procedures reveal the formation of a HP incorporating NaV1.7's CC and AG. We report on two "hot" map areas attracting pain-related mutation sites distributed along HP's boundary. Probing the SOC hypothesis for HIs around NaV1.7's pore reveals that "hot" structural locations tend to cluster at a distance of ~ 33.4 Å from the SF. Stability implications of these observations can be deduced by considering that in the vicinity of the critical point the range and intensity of HIs increase in a power-law fashion thus favoring amplification and propagation of mutation-induced perturbations peripherally to the HP and at critical HIs-distance from the SF thus not directly affecting neither of them. The clinical translational value of our findings is tested by predicting pathogenicity of 84 NaV1.7 variants; a weighted average of HP- and SF-related distance metrics can classify up to 29 (out of 36) pain-related variants and 45 (out of 48) neutral variants correctly.

Methods

All computations were performed in R [73] environment unless stated differently.

3D structure preparation

The NaV1.7 atomic structural model used throughout this study was constructed via homology modeling procedures based on the pre-open NaVAb template [PDB code: 3RVY] [74] according to [7]. In short, the first step undertaken was to generate structural models of the four transmembrane domains (DI-DIV) by utilizing the membrane-bound protein prediction algorithm GPCR-ITASSER [75–77]. Then, each domain was aligned upon the pre-open NaVAb template by using the TM-align algorithm [78]. Finally, the four transmembrane domains were placed together in a clockwise order viewed from extracellular side (ES) according to [79, 80], and the resulting four domain complex structural model was refined by fragment-guided molecular dynamics simulations aiming at removing interdomain clashes, optimizing hydrogen atoms network, and, consequently, increasing model quality [75, 76, 81]. The retrieved model consists of 1140 protonated amino acids (DI: P229:K417, DII: P839:T972, DIII: M1296:G1461, DIV: K1617:T1763). A comparison via superposition of the retrieved model with a recently resolved cryo-electron microscopy (cryo-EM) NaV1.7 structure [PDB code: 6J8J] [82] is presented in Additional file 1: S1.

In continuation, principal axes of the NaV1.7 model structure were estimated by using the VMD software [83]. A global coordinate system ($\hat{x}, \hat{y}, \hat{z}$) was introduced with its center at O and the NaV1.7's principal pore axis, i.e., the axis approximating the direction of the channel's pore, was aligned with the z -axis with orientation from the ES toward the intracellular side (IS) with respect to \hat{z} . The atomic center $\mathbf{e} = \frac{1}{M} \sum_{i=1}^{N_c} m_i \cdot \mathbf{c}_i$ of the

3D structure was set to overlap with O , where $\mathbf{c}_i = (c_{x,i}, c_{y,i}, c_{z,i})$ is the atomic center of the i th atom, m_i is the mass of the i th atom, $N_c = 18567$ is the total number of atoms, and $M = \sum_{i=1}^{N_c} m_i$ is the total molecular mass (values of atomic masses are the same as [68, 69]).

Geometrical characteristics of the pore

We navigated through the skewed NaV1.7's pore by introducing a set of pore points $\mathbf{p} \in P$ (see Additional file 1: S2). The pore radius at \mathbf{p} is given by [?]

$$R(\mathbf{p}) = \min_{i=1,2,\dots,N_c} \{ \|\mathbf{c}_i - \mathbf{p}\| - vdW_i \} \tag{m2}$$

where $\|\cdot\|$ is the euclidean norm and vdW_i is the van der Waals radius of the i th atom (values of van der Waals radii are the same as [68, 69]). The distance between \mathbf{p} and its nearest neighbor atom corresponds then to

$$D(\mathbf{p}) = \min_{i=1,2,\dots,N_c} \{ \|\mathbf{c}_i - \mathbf{p}\| \} \tag{m3}$$

and the outer surface radius at \mathbf{p} is given by [68, 69]

$$L(\mathbf{p}) = \max_{i=1,2,\dots,N_c} \{ \|\mathbf{c}_i - \mathbf{p}\| + vdW_i \} \tag{m4}$$

where the unit of measurement for $R(\mathbf{p})$, $D(\mathbf{p})$ and $L(\mathbf{p})$ is expressed in [Å].

Finite-size sampling around the pore

The atomic environment around \mathbf{p} is sampled with concentric spheres placed at \mathbf{p} of increasing radius [68, 69]

$$l_\alpha(\mathbf{p}) = D(\mathbf{p}) + \alpha \cdot \frac{L(\mathbf{p}) - D(\mathbf{p})}{K_\alpha} \text{ for } \alpha = 1, 2, \dots, K_\alpha \rightarrow \infty \tag{m5}$$

where K_α is the total number of sampling spheres and α denotes the index of the sampling sphere (i.e., the scaling index). $l_\alpha(\mathbf{p})$ indicates the size, i.e., molecular scale, of the spherical cluster of atoms around \mathbf{p} in [Å] and $L(\mathbf{p})$ the finite channel size measured with respect to \mathbf{p} . Accordingly, the atomic cumulative distribution function (CDF) at \mathbf{p} is given by [68, 69]

$$N(\mathbf{p}, l_\alpha(\mathbf{p})) = \sum_{i=1}^{N_c} \theta(l_\alpha(\mathbf{p}) - \|\mathbf{c}_i - \mathbf{p}\|) \tag{m6}$$

where $\theta(\cdot)$ is the heaviside function. Note that $N(\mathbf{p}, l_\alpha(\mathbf{p}))$ essentially describes how atoms are packed around \mathbf{p} . In computational practice K_α is set to be “large enough” approximating the continuous case via dense sampling.

Mathematical modeling of atomic CDF

Modeling of the atomic CDF was performed by employing the GROFIT routine [84]. Hypothesis underlying this modeling approach is that the atomic CDF for a given \mathbf{p} follows a sigmoid pattern. Hypothesis is approved if GROFIT manages to fit any of available

candidate models to the CDF data. Available candidate models are a re-parametrized algebraic forms [85] of the Logistic model [86]

$$n_{LOG}(\mathbf{p}, l_\alpha(\mathbf{p})) = A(\mathbf{p}) \cdot \left\{ 1 + \exp\left(\frac{A \cdot t(\mathbf{p})}{A(\mathbf{p})} \cdot (s(\mathbf{p}) - l_\alpha(\mathbf{p})) + 2\right) \right\}^{-1} \tag{m7}$$

, of the Gompertz model [87]

$$n_{GOM}(\mathbf{p}, l_\alpha(\mathbf{p})) = A(\mathbf{p}) \cdot \exp\left(-\exp\left(\frac{e \cdot t(\mathbf{p})}{A(\mathbf{p})} \cdot (s(\mathbf{p}) - l_\alpha(\mathbf{p})) + 1\right)\right) \tag{m8}$$

with $e = \exp(1)$, of the the modified Gompertz model [85]

$$n_{MGOM}(\mathbf{p}, l_\alpha(\mathbf{p})) = A(\mathbf{p}) \cdot \exp\left(-\exp\left(\frac{e \cdot t(\mathbf{p})}{A(\mathbf{p})} \cdot (s(\mathbf{p}) - l_\alpha(\mathbf{p})) + 1\right)\right) + A(\mathbf{p}) \cdot \exp(w(\mathbf{p}) \cdot (l_\alpha(\mathbf{p}) - l_{shift}(\mathbf{p}))) \tag{m9}$$

and of the Richards model [88]

$$n_{RIC}(\mathbf{p}, l_\alpha(\mathbf{p})) = A(\mathbf{p}) \cdot \{1 + \tilde{q}(\mathbf{p}) \cdot b(\mathbf{p}) \cdot \exp(-k(\mathbf{p}) \cdot l_\alpha(\mathbf{p}))\}^{-1/\tilde{q}(\mathbf{p})}$$

with $b(\mathbf{p}) = \exp(1 + \tilde{q}(\mathbf{p}) + k(\mathbf{p}) \cdot s(\mathbf{p}))$ and $k(\mathbf{p}) = \frac{t(\mathbf{p})}{A(\mathbf{p})} \cdot (1 + \tilde{q}(\mathbf{p}))^{1+1/\tilde{q}(\mathbf{p})}$

$$\tag{m10}$$

were fitted on $N(\mathbf{p}, l_\alpha(\mathbf{p}))$ along $l_\alpha(\mathbf{p})$ -direction where $\{A(\mathbf{p}), t(\mathbf{p}), s(\mathbf{p}), \tilde{q}(\mathbf{p}), w(\mathbf{p}), l_{shift}(\mathbf{p})\}$ are model parameters. The candidate model that best fits the atomic CDF is then selected based on minimization of an Akaike information criterion (see [84] for algorithmic details).

Following [69], model parameters interpretation was performed with respect to the inflection point

$$\xi(\mathbf{p}) = \{l_\alpha(\mathbf{p}) \mid \frac{\partial^2 n(\mathbf{p}, l_\alpha(\mathbf{p}))}{\partial l_\alpha(\mathbf{p})^2} = 0\} \tag{m11}$$

that determines the location along $l_\alpha(\mathbf{p})$ -direction where the radial distribution function (RDF), $\frac{\partial n(\mathbf{p}, l_\alpha(\mathbf{p}))}{\partial l_\alpha(\mathbf{p})}$, maximizes. The RDF maximum value is given by the parameter $t(\mathbf{p})$ accounting for the maximum atom-packing rate (or, equivalently, for the maximum atomic density) around \mathbf{p} . Parameter $A(\mathbf{p})$ is the asymptote value of the fitted model, i.e., $n(\mathbf{p}, l_\alpha(\mathbf{p}) \rightarrow \infty) = A(\mathbf{p})$, describing what happens when $L(\mathbf{p})$ becomes arbitrary large. Parameter $s(\mathbf{p})$ determines the location along $l_\alpha(\mathbf{p})$ -direction where the lag atom-packing domain ends, i.e., its size. Notably, parameter $t(\mathbf{p})$ can be expressed in terms of the ratio $t(\mathbf{p}) = \frac{A(\mathbf{p})}{os(\mathbf{p}) := o(\mathbf{p}) - s(\mathbf{p})}$ with $o(\mathbf{p})$ determining the location along $l_\alpha(\mathbf{p})$ -direction where the asymptote atom-packing domain begins. Parameter $\tilde{q}(\mathbf{p})$ affects the shape of the Richards model curve, as well as, the location of the inflection point thus plays the role of the summary atom-packing parameter. Parameters $w(\mathbf{p})$, and $l_{shift}(\mathbf{p})$ of the modified Gompertz model indicate the location, and the slope, respectively, of a second increase in the modified Gompertz model curve [84]. The Logistic and the Gompertz model are retrieved from the Richards model for $\tilde{q}(\mathbf{p}) = 1$, and for $\tilde{q}(\mathbf{p}) \rightarrow 0$, respectively, as shown in [89], thus they are considered as special cases of the Richards model.

Cumulative hydrophobicity-property functions

The hydrophobic density of the atomic environment around \mathbf{p} was approximated in terms of [68]

$$m^{(0)}(\mathbf{p}, l_\alpha(\mathbf{p})) = \frac{h^{(0)}(\mathbf{p}, l_\alpha(\mathbf{p}))}{N(\mathbf{p}, l_\alpha(\mathbf{p}))} \sim \text{kcal}/(\text{mol} \equiv \text{atom})$$

$$\text{with } h^{(0)}(\mathbf{p}, l_\alpha(\mathbf{p})) = \sum_{i=1}^{N_c} \theta(l_\alpha(\mathbf{p}) - \|\mathbf{c}_i - \mathbf{p}\|) \cdot HI_i^w$$
(m12)

where $h^{(0)}(\mathbf{p}, l_\alpha(\mathbf{p}))$ corresponds to the cumulative zero-order hydrophobic pore moment function [90] with $HI_i^w = HI_i + w_i$ representing the i th atomic hydrophobic index in accordance with the Kapcha&Rosky atomic hydrophobic scale [91] with additive Gaussian noise $w_i \in \mathcal{N}(\mu = 0, \sigma = 0.001)$. The superscript “(0)” indicates the moment order.

The hydrophobic interatomic interaction strength (HIIS) at \mathbf{p} , i.e., the average interaction strength between an atomic component found within the cluster of size $N(\mathbf{p}, l_\alpha(\mathbf{p}))$ and its surroundings, was approximated in terms of the hydrophobic imbalance (or interaction strength) pore function [68, 69]

$$\vec{m}^{(1)}(\mathbf{p}, l_\alpha(\mathbf{p})) = \frac{\vec{h}^{(1)}(\mathbf{p}, l_\alpha(\mathbf{p}))}{N(\mathbf{p}, l_\alpha(\mathbf{p}))} \sim \text{kcal} \cdot \text{\AA}/(\text{mol} \equiv \text{atom})$$

$$\text{with } \vec{h}^{(1)}(\mathbf{p}, l_\alpha(\mathbf{p})) = \sum_{i=1}^{N_c} \theta(l_\alpha(\mathbf{p}) - \|\mathbf{c}_i - \mathbf{p}\|) \cdot HI_i^w \cdot \vec{r}_{\mathbf{p},i}$$

$$= \underbrace{h_x^{(1)}(\mathbf{p}, l_\alpha(\mathbf{p})) \cdot \hat{\mathbf{x}} + h_y^{(1)}(\mathbf{p}, l_\alpha(\mathbf{p})) \cdot \hat{\mathbf{y}}}_{\vec{h}_{xy}^{(1)}(\mathbf{p}, l_\alpha(\mathbf{p}))} + \underbrace{h_z^{(1)}(\mathbf{p}, l_\alpha(\mathbf{p})) \cdot \hat{\mathbf{z}}}_{\vec{h}_z^{(1)}(\mathbf{p}, l_\alpha(\mathbf{p}))}$$
(m13)

where $\vec{h}^{(1)}(\mathbf{p}, l_\alpha(\mathbf{p}))$ corresponds to the cumulative first-order hydrophobic pore moment function [90] quantifying the hydrophobic inter-cluster interaction strength (HICIS) with $\vec{r}_{\mathbf{p},i}$ being the vector from \mathbf{p} to \mathbf{c}_i . The superscript “(1)” indicates the moment order.

Introduction of a weak noise source w_i practically guarantees that scalars $|h^{(0)}(\mathbf{p}, l_\alpha(\mathbf{p}))|$ and $\|\vec{h}^{(1)}(\mathbf{p}, l_\alpha(\mathbf{p}))\|$ are non-zero for every combination of \mathbf{p} and $l_\alpha(\mathbf{p})$ while their scaling behavior remains practically unaffected. Throughout this study we consider pore’s physicochemical field characteristics to be adequately described in terms of the HIIS axial field component, $\vec{m}_z^{(1)}(\mathbf{p}, l_\alpha(\mathbf{p})) = \vec{h}_z^{(1)}(\mathbf{p}, l_\alpha(\mathbf{p}))/N(\mathbf{p}, l_\alpha(\mathbf{p})) = m_z^{(1)}(\mathbf{p}, l_\alpha(\mathbf{p})) \cdot \hat{\mathbf{z}}$ given that the magnitude of the radial field component, $\|\vec{h}_{xy}^{(1)}(\mathbf{p}, l_\alpha(\mathbf{p}))\|$, is statistically expected to remain always smaller than $\|\vec{m}_z^{(1)}(\mathbf{p}, l_\alpha(\mathbf{p}))\|$ after a cut-off, lag-domain scale and, thereafter, to gradually shrink (see Additional file 1: S3). Accordingly, we focus only on the scaling behavior and topology of the HIIS axial field component which can occupy only two orientation-states; an “in” orientation-state which is characterized by $\vec{m}_z^{(1)}(\mathbf{p}, l_\alpha(\mathbf{p}))$ pointing towards the intracellular side (IS), i.e., by $m_z^{(1)}(\mathbf{p}, l_\alpha(\mathbf{p})) > 0$, and an “out” orientation-state which is characterized by $\vec{m}_z^{(1)}(\mathbf{p}, l_\alpha(\mathbf{p}))$ pointing towards the ES, i.e., by $m_z^{(1)}(\mathbf{p}, l_\alpha(\mathbf{p})) < 0$. Topological changes in HIIS axial field component are detected according to the algorithmic scheme presented in [68] (see Additional file 1: S4).

Finite-size scaling of HIIS axial field component

In accordance to [69], a scale-invariant interval of the HIIS axial field component corresponds to combinations of \mathbf{p} with α for which the power-law approximation

$$\|\vec{h}_z^{(1)}(\mathbf{p}, l_\alpha(\mathbf{p}))\| \sim l_\alpha(\mathbf{p})^{\gamma(\mathbf{p})} \quad (\text{m14})$$

is accurately satisfied indicating that HIIS axial field component stabilizing the cluster of $N(\mathbf{p}, l_\alpha(\mathbf{p}))$ atoms around \mathbf{p} span a range up to $\sim l_\alpha(\mathbf{p}) \text{ \AA}$. Sign of $\gamma(\mathbf{p})$ quantifies the rate at which intensity and range of HIIS axial field component increase or decrease for increasing atomic cluster size. From a HIs-network standpoint, $\gamma(\mathbf{p})$ indicates whether HIs network interconnectivity is up- or down-regulated, i.e., whether HIs contacts, e.g., hydrogen bonds, are created or destroyed within the structure. The energy levels associated with HIs contacts creation (or destruction) guaranteeing stability of the atomic cluster can then be approximated by

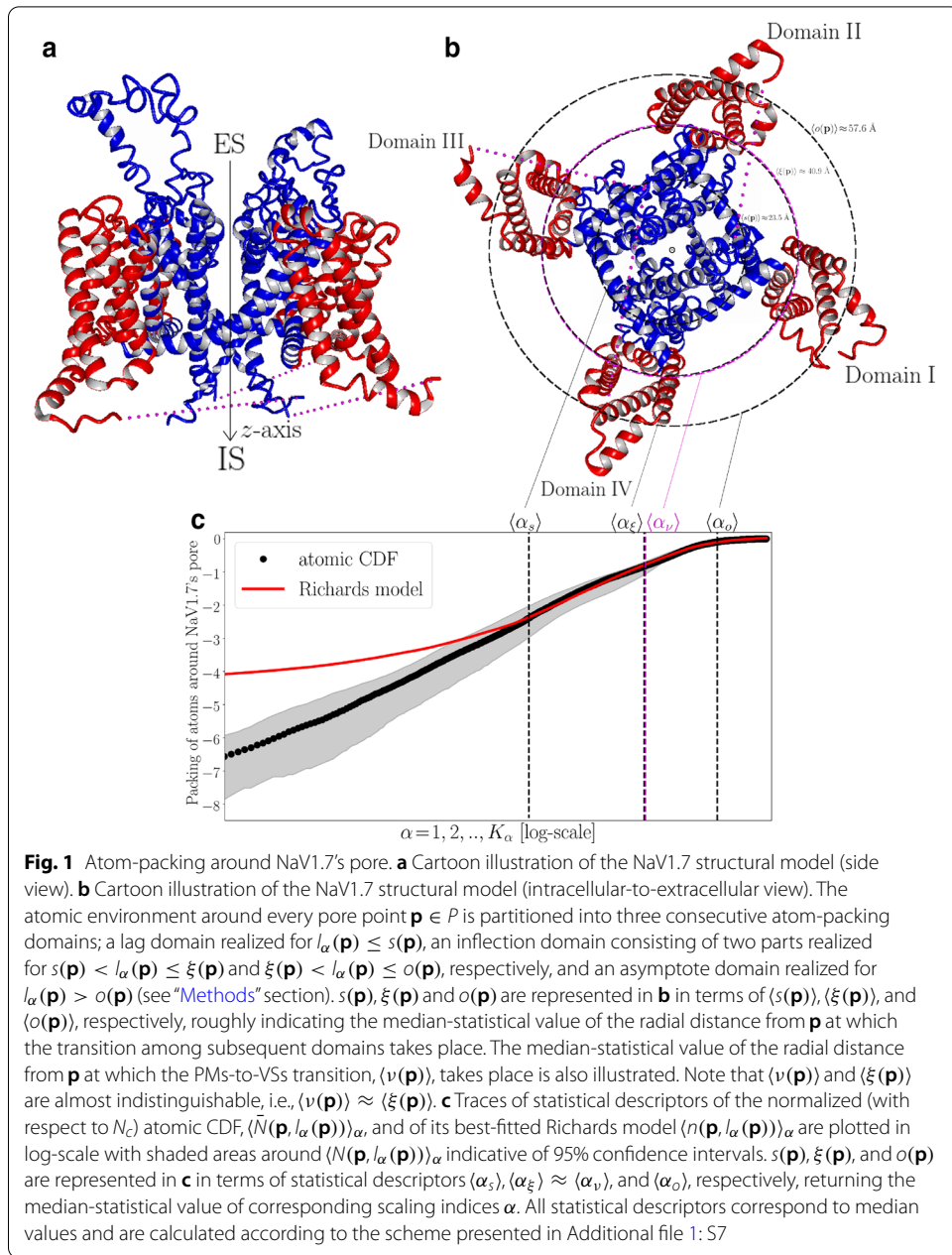
$$U(\mathbf{p}, l_\alpha(\mathbf{p})) = \|\vec{h}_z^{(1)}(\mathbf{p}, l_\alpha(\mathbf{p}))\|/l_\alpha(\mathbf{p}) \sim N(\mathbf{p}, l_\alpha(\mathbf{p})) \cdot l_\alpha(\mathbf{p})^{\gamma(\mathbf{p})-1} \quad (\text{m15})$$

measured in kcal/(mol \equiv atomic cluster).

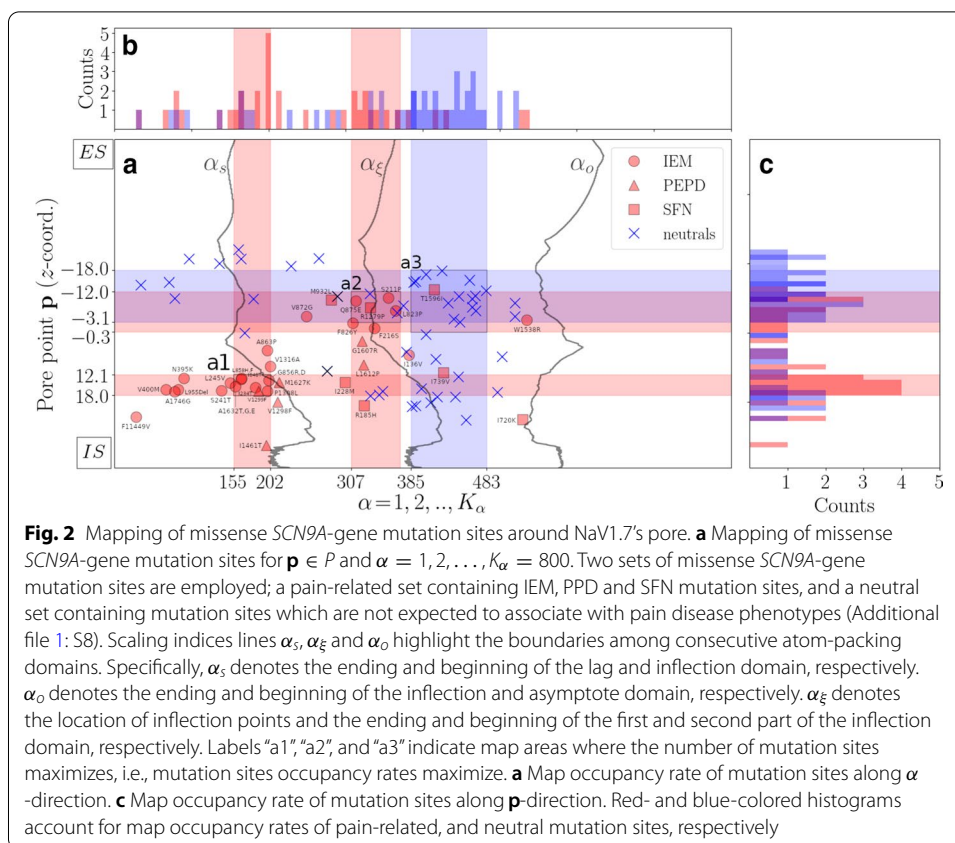
Results

In Fig. 1 we demonstrate that atomic CDF around Nav1.7's pore follows a sigmoid profile which can be adequately described by the Richards model (Additional file 1: S5). The atomic environment around the pore can thus be partitioned into three consecutive atom-packing domains spanning the channel from the inside (i.e., pore-lining environment) to the outside (i.e., voltage-sensing environment) (Fig. 1b, c). The innermost domain corresponds to the lag domain consisting primarily of structural elements lining the pore (approximately 95% of lag-domain structural components belong to S5–S6 helices). The outermost domain corresponds to the asymptote domain consisting mostly of structural elements drawn from the S1–S4 voltage-sensing helices (approximately 63.3% of asymptote-domain structural components belong to the S1–S4 helices). In-between the lag and asymptote domain, a structurally-heterogeneous inflection domain is formed consisting of two parts separated by inflection points, $\xi(\mathbf{p})$. Structural locations of the inflection points correspond to intra-channel regions where the atomic RDF maximizes and, as demonstrated in Fig. 1a, they closely match the PMs-VSs spatial transition described by $\nu(\mathbf{p})$ (see Additional file 1: S6 for calculation of PMs-VSs spatial transition characteristics). Accordingly, $\xi(\mathbf{p})$ serves here as a macroscopic boundary line splitting the atomic environment around Nav1.7's pore into two phases, namely, a pre-inflection phase for $l_\alpha(\mathbf{p}) \leq \xi(\mathbf{p})$ and a post-inflection phase for $l_\alpha(\mathbf{p}) > \xi(\mathbf{p})$ accounting for atomic sub-environments containing mainly structural components belonging to the PMs and VSs, respectively (Fig. 1b).

Based on the geometrical partition scheme summarized in Fig. 1 we proceeded with mapping of missense SCN9A-gene mutations on two-dimensions based on their intra-channel structural locations. For that, we utilized a collection of well-studied GOF Nav1.7 mutations phenotypically related with IEM, SFN and PEPD pain disease



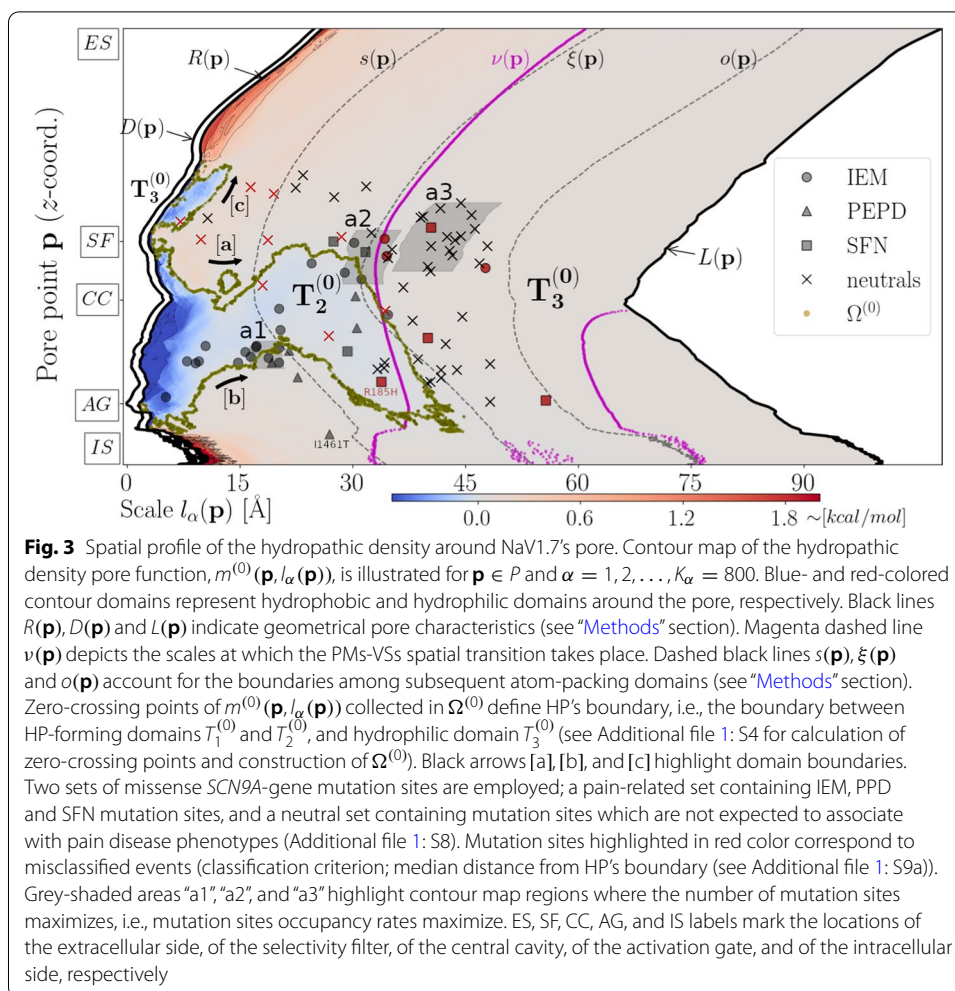
(total number of pain-related mutation sites: 36) (Additional file 1: S8). In addition, a collection of neutrals *SCN9A*-gene mutations was introduced consisting of *SCN9A*-gene homologous single-nucleotide polymorphisms (hSNPs) and of *SCN9A*-gene variants not causing biophysical abnormalities (nBABNs) (imported from [59]), as well as, of a small number of *SCN9A*-gene variants previously classified as non-pathogenic based on algorithmic procedures described in [92] (total number of neutral mutation sites: 48) (Additional file 1: S8). Given that neutrals are not expected to associate with pain disease phenotypes, they are less likely to trigger any significant NaV1.7



destabilizations and/or to perturb conserved hydrophobic characteristics around NaV1.7's pore.

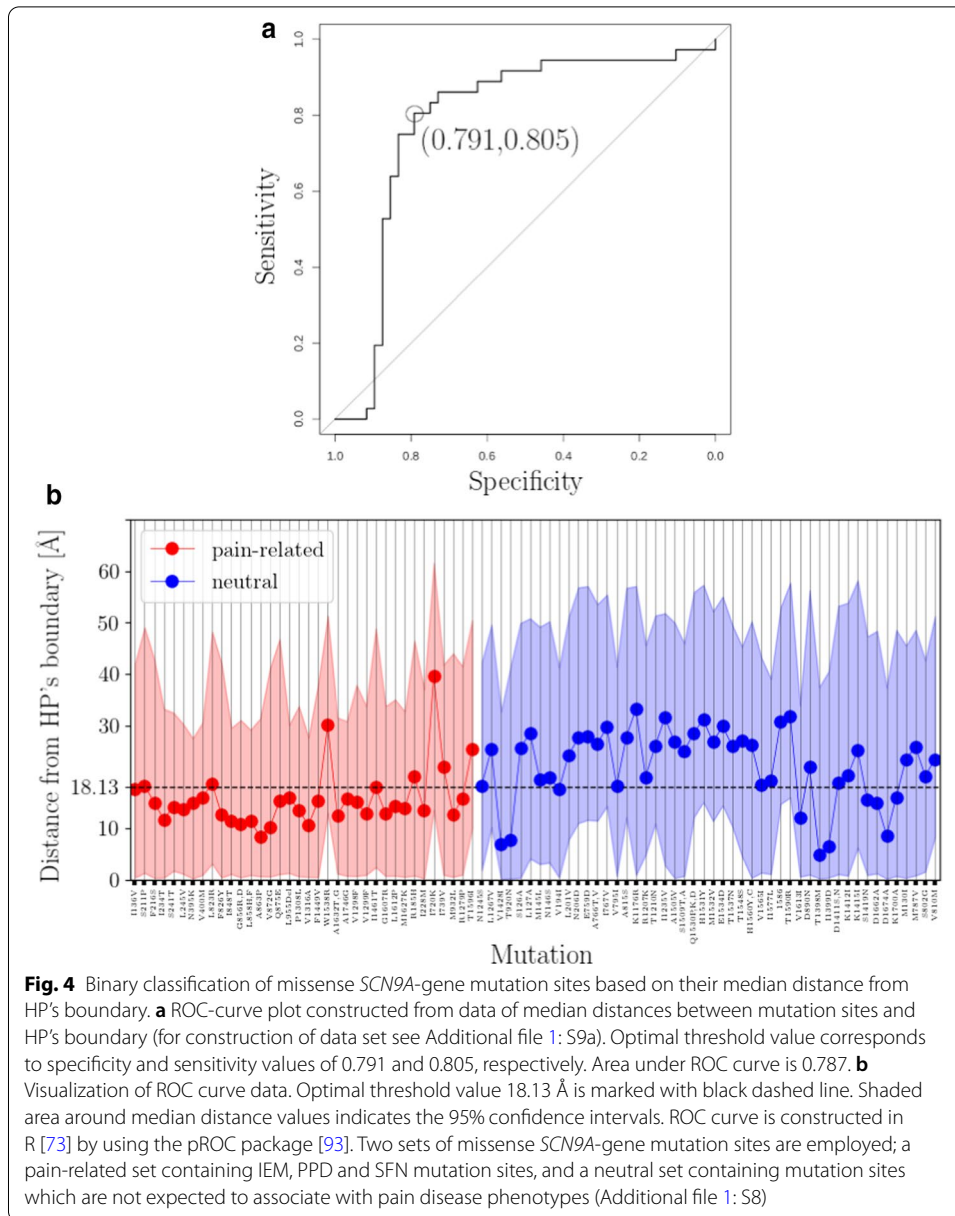
The majority (i.e., 54%) of pain-related mutation sites are distributed within the inflection domain with a tendency to cluster toward a centrally-located map area along the inflection-points line α_ϵ (see area "a2" on Fig. 2a in relation to Fig. 2b, c). On the other hand, the majority (i.e., 75%) of neutral mutation sites are distributed within the second part of the inflection domain so that their map occupancy rate tends to maximize approximately in the middle of the second part of the inflection domain (see area "a3" on Fig. 2a in relation to Fig. 2b, c). The rest 46% of pain-related mutation sites are found within the lag domain toward the intracellular side of the NaV1.7. In particular, their map occupancy rate maximizes in the vicinity of the boundary line α_s toward the IS (see area "a1" on Fig. 2a in relation to Fig. 2b, c). Taken together, these observations indicate that for decreasing molecular scale the probability of a missense *SCN9A*-gene mutation to translate into a pain-related phenotype increases which is of little surprise considering that mutations perturbing NaV1.7's interior are more likely to perturb tight packing of S5-S6 helices and, consequently, produce electrophysiological alternations.

Mapping of hydrophobic density profile reveals the formation of a HP lining NaV1.7's pore (see Fig. 3, blue-colored domains $T_1^{(0)}$ and $T_2^{(0)}$). Specifically, we demonstrate that the center of the pore is lined by predominantly hydrophobic atomic components expanding toward the IS where occlusion of the pore takes place by the ring of Y405 (DI), F960 (DII) F1449 (DIII) and F1752 (DIV) residues which are known to form the



NaV1.7's activation gate (AG) (see Fig. 3, blue-colored domain $T_2^{(0)}$). Hydrophobic expansion toward the ES is disrupted by the weakly-hydrophilic SF so that the pore is lined by a small-sized hydrophobic cluster located in-between the strongly-hydrophilic ES mouth and the weakly-hydrophilic SF (see Fig. 3, blue-colored domain $T_1^{(0)}$). Macroscopically, the wide CC translates into a structural contraction event as the outer surface radius is locally minimized so that the channel is split into two funnel-like structural compartments (see Fig. 3, trace of $L(\mathbf{p})$). Structural combination of the PMs with the VSs results in a hydrophilic atomic environment as indicated by the red-colored $T_3^{(0)}$ domain covering the largest map area and incorporating both the SF and the ES mouth, as well as, the IS channel end (see Fig. 3). The SF's microenvironment is formed by the residues D361 (DI), E930 (DII), K1406 (DIII) and A1698 (DIV) where a bare sodium ion of radius $\sim 1.8 \text{ \AA}$ can exactly fit in (Fig. 3).

Strikingly, approximately 53% of pain-related mutation sites are found within $T_2^{(0)}$ with a tendency to cluster along HP's boundary as map areas “a1” and “a2” occupy contour map regions where the transition from $T_2^{(0)}$ to $T_3^{(0)}$ takes place (Fig. 3). On the other hand,



10% of neutral mutation sites are located within the $T_2^{(0)}$ and only one neutral mutation site found within $T_1^{(0)}$, while area “a3” is distributed solely within $T_3^{(0)}$ (Fig. 3).

Given that mutations perturbing an ion channel’s hydrophobic interior properties pose a high risk for ion current alternations [53–56], we hypothesize that mutations occurring at structural locations in proximity to the HP are more likely to be related with GOF pain phenotypes. We tested this hypothesis by statistically approximating the distance between each mutation structural location and HP’s boundary (Additional file 1: S9a) and feeding retrieved median distances into a binary classifier. We achieved to classify correctly 29 (out of 36) and 38 (out of 48) of pain-related and neutral, respectively,

mutations correctly with a cut-off median distance of 18.13 Å (Fig. 4). This translates to an area under receiver operating characteristics (ROC) curve of 0.787 and pain phenotype prediction with specificity of 0.791 and sensitivity of 0.805 (Fig. 4a).

Misclassified pain-related mutations S211P, L823R, W1538R, I720K, I739V and T1596I are found outside of the HP thus not in hydrophobic proximity neither to CC nor to AG (Figs. 3 and 4b). Only a single pain-related misclassification is found within HP, namely, R185H that is located with $T_2^{(0)}$ (Figs. 3 and 4b). This striking misclassification is due to the elementary statistical approach adopted for calculating distance scores which fails to fully capture the complex topology of HP-forming $T_2^{(0)}$ and $T_1^{(0)}$ (Additional file 1: S8). Misclassified neutral mutations V1428I, T920N, V194I, V1613I, T1398N, I1399D, S1419N, D1662A, D1674A and K1700A are found inside the HP, and, more precisely, in proximity to HP’s boundary, with a tendency to cluster around the SF (Figs. 3 and 4b).

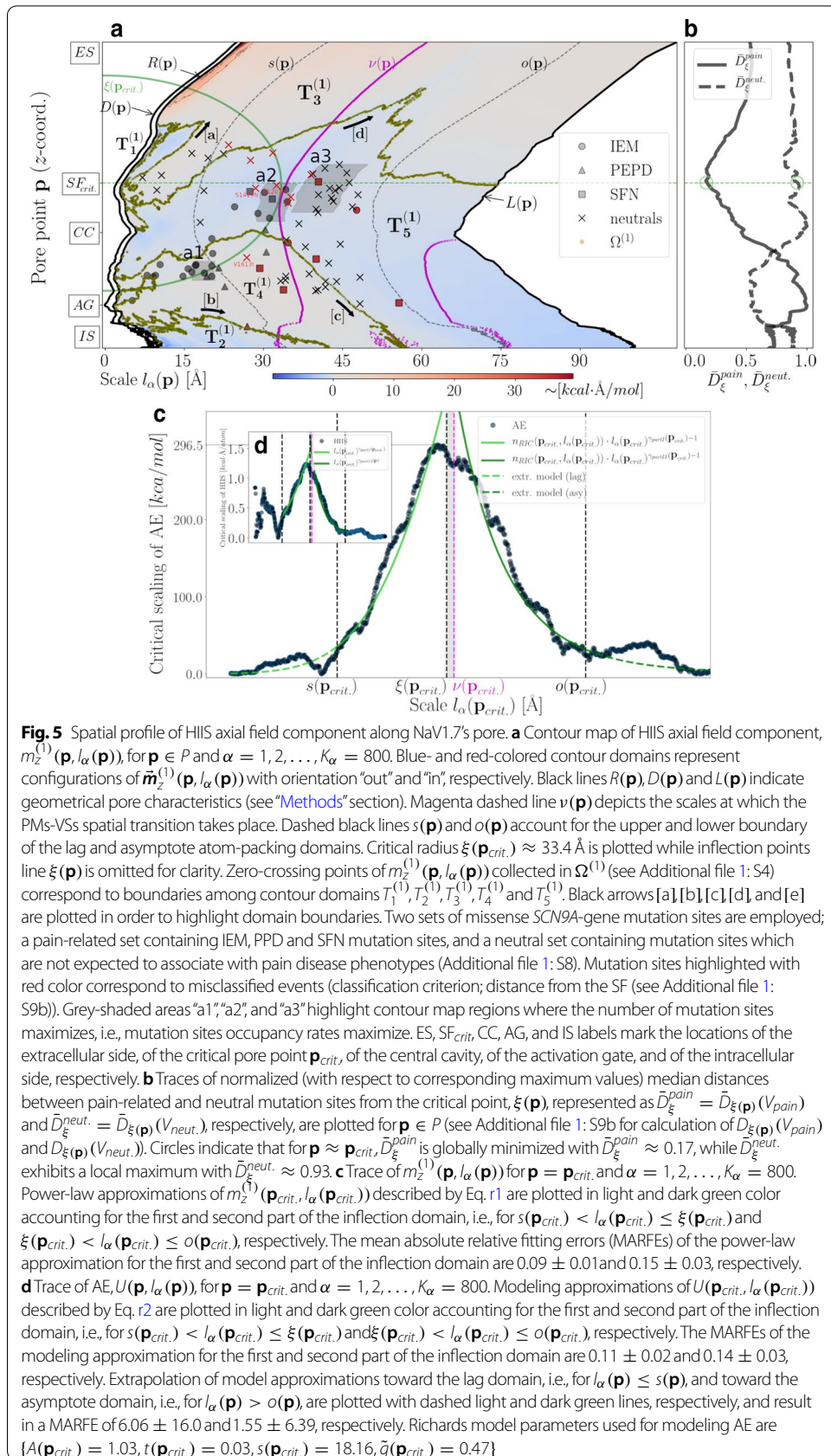
We further investigated the relation between cumulative hydrophobic characteristics and mutation sites around NaV1.7’s pore by focusing on the HIIS axial field component illustrated in Fig. 5a. As we demonstrate in Fig. 5a, HIIS axial field component topology can be summarized into five domains, namely, $T_1^{(1)}$, $T_2^{(1)}$, $T_3^{(1)}$, $T_4^{(1)}$ and $T_5^{(1)}$ (Fig. 5a). The centrally-located $T_5^{(1)}$ domain covers the largest map area and roughly dichotomizes the contour map into two pseudo-symmetric parts, namely, an ES part incorporating $T_1^{(1)}$ and $T_3^{(1)}$, and an IS part incorporating $T_2^{(1)}$ and $T_4^{(1)}$. Pain-related mutation sites are solely found within the $T_4^{(1)}$ and $T_5^{(1)}$ domains with occupancy rates of 58% and 42%, respectively. On the other hand, neutral sites are found within the $T_3^{(1)}$, $T_4^{(1)}$ and $T_5^{(1)}$ with occupancy rates of 14%, 19% and 67%, respectively.

In order to decode mutation sites clustering behavior on the contour map of Fig. 5a we adopted a phenomenological approach that presumes the existence of a critical point, $\xi(\mathbf{p}_{crit.})$, associated with the spatial organization of HIs around the SF [63, 64, 69] with $\mathbf{p}_{crit.}$ being a critical SF pore point coordinate (Additional file 1: S10). A crucial result that motivated us to adopt such an approach is that pain-related mutation sites are attracted toward the critical point in sheer contrast to neutral mutation sites which are repelled from it (Fig. 5b). We refer to this phenomenon with the term critical clustering. Geometrically, the formation of the critical mutation-sites cluster reflects the tendency of structural locations of pain-related mutations to minimize their distance from the surface of the sphere of radius $\xi(\mathbf{p}_{crit.}) \approx 33.4 \text{ \AA}$ around the SF; intuitive graphical representation of this phenomenon is provided in Fig. 5a where we show that “hot” areas I and II intersect with the green radius line $\xi(\mathbf{p}_{crit.})$ representing critical sphere’s surface.

The scaling behavior of HIIS axial field component around $\mathbf{p}_{crit.}$ is adequately described in terms of the power-law scheme

$$m_z^{(1)}(\mathbf{p}_{crit.}, l_\alpha(\mathbf{p}_{crit.})) \sim \begin{cases} l_\alpha(\mathbf{p}_{crit.})^{\gamma_{partI}(\mathbf{p}_{crit.})} & \text{for } s(\mathbf{p}_{crit.}) < l_\alpha(\mathbf{p}_{crit.}) \leq \xi(\mathbf{p}_{crit.}) \\ l_\alpha(\mathbf{p}_{crit.})^{\gamma_{partII}(\mathbf{p}_{crit.})} & \text{for } \xi(\mathbf{p}_{crit.}) < l_\alpha(\mathbf{p}_{crit.}) \leq o(\mathbf{p}_{crit.}) \end{cases} \quad (r1)$$

accounting for a HIs-network expansion and contraction within the pre- and post-inflection phase intervals $s(\mathbf{p}_{crit.}) < l_\alpha(\mathbf{p}_{crit.}) \leq \xi(\mathbf{p}_{crit.})$ and $\xi(\mathbf{p}_{crit.}) < l_\alpha(\mathbf{p}_{crit.}) \leq o(\mathbf{p}_{crit.})$ with rates of $\gamma_{partI}(\mathbf{p}_{crit.}) = 2.27 \pm 0.18$ and $\gamma_{partII}(\mathbf{p}_{crit.}) = -5.18 \pm 1.02$, respectively (Fig. 5c, and see also Additional file 1: S10). On the left of the interval



$\xi(\mathbf{p}_{crit.}) < l_\alpha(\mathbf{p}_{crit.}) \leq \nu(\mathbf{p}_{crit.})$, both, the range and intensity of HII axial field component maximize as the HIs-network configuration exceeds its critical size marking the transition from the pre-inflection phase toward the post-inflection phase [69]. The energy levels associated with this phase transition are given by

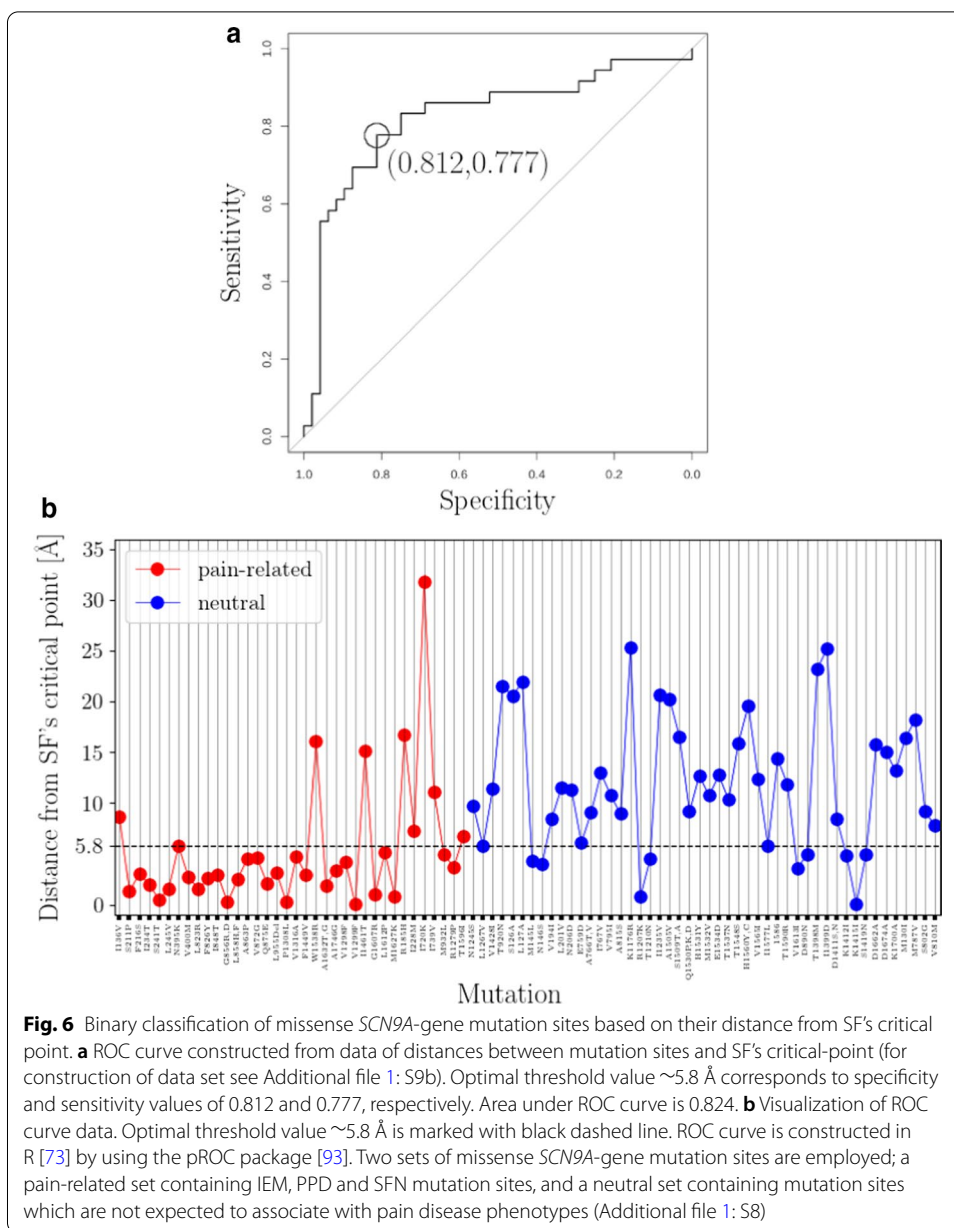
$$U(\mathbf{p}_{crit.}, l_\alpha(\mathbf{p}_{crit.})) \sim \begin{cases} N(\mathbf{p}_{crit.}, l_\alpha(\mathbf{p}_{crit.})) \cdot l_\alpha(\mathbf{p}_{crit.})^{\gamma_{partI}(\mathbf{p}_{crit.})-1} & \text{for } s(\mathbf{p}_{crit.}) < l_\alpha(\mathbf{p}_{crit.}) \leq \xi(\mathbf{p}_{crit.}) \\ N(\mathbf{p}_{crit.}, l_\alpha(\mathbf{p}_{crit.})) \cdot l_\alpha(\mathbf{p}_{crit.})^{\gamma_{partII}(\mathbf{p}_{crit.})-1} & \text{for } \xi(\mathbf{p}_{crit.}) < l_\alpha(\mathbf{p}_{crit.}) \leq o(\mathbf{p}_{crit.}) \end{cases} \quad (r2)$$

where $N(\mathbf{p}_{crit.}, l_\alpha(\mathbf{p}_{crit.}))$ can be replaced with its best-fitted Richards model, $n_{ric}(\mathbf{p}_{crit.}, l_\alpha(\mathbf{p}_{crit.}))$ (see caption of Fig. 5 for Richards model parameters), providing with an estimation of the atom-packing energy (AE) (Fig. 5c). Similarly to the NaVAb case [69], AE maximization occurs in the vicinity of the narrow interval $[\xi(\mathbf{p}_{crit.}), \nu(\mathbf{p}_{crit.})]$ so that energetic coupling of the PMs with the VSs is dictated by the phase transition (Fig. 5c, d).

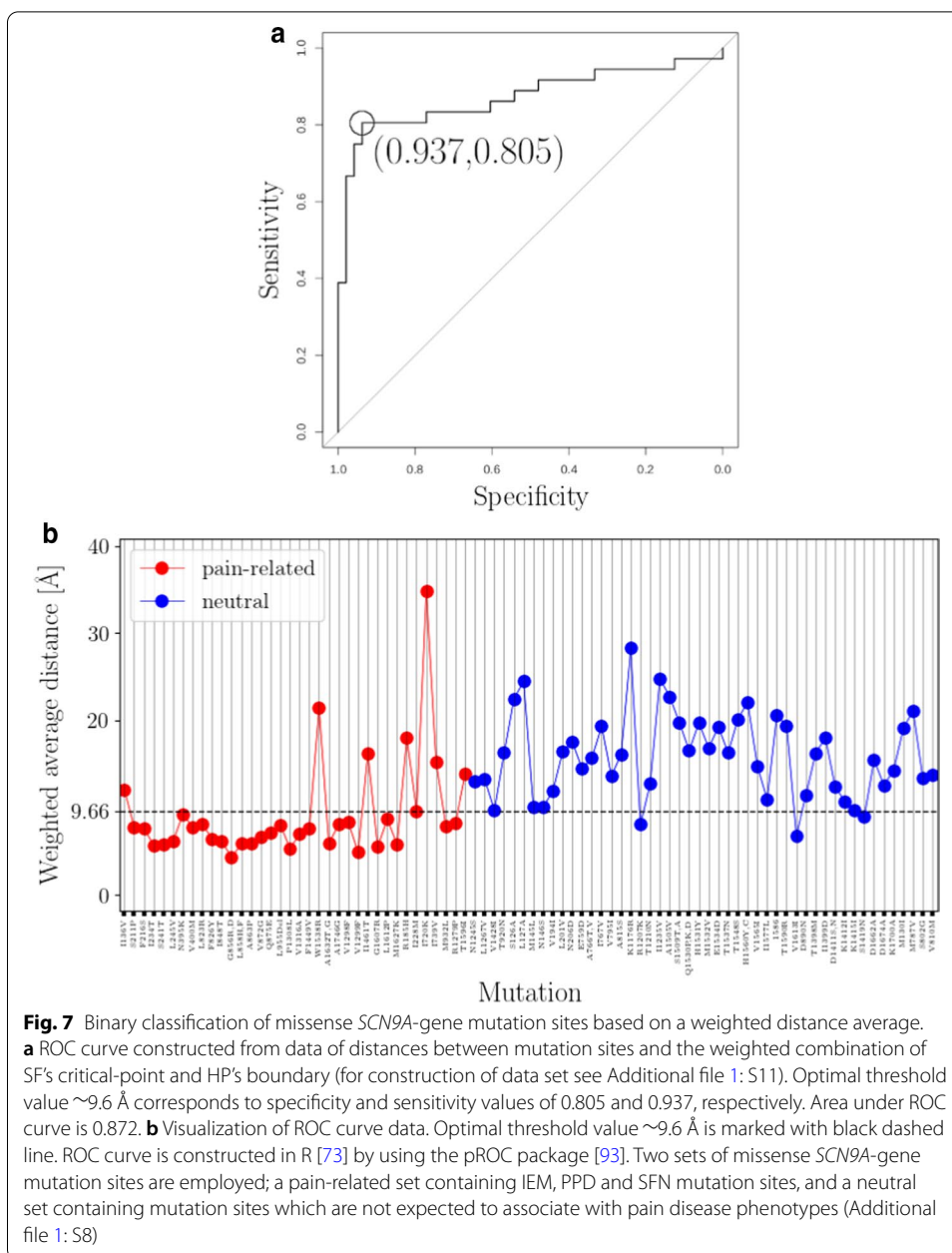
Equation r1 indicates that interatomic HIs law is robust to microscopic modifications of the atomic structure, e.g., addition, removal or deletion of a small number of atoms occurring due to a mutation-induced perturbation of $N(\mathbf{p}_{crit.}, l_\alpha(\mathbf{p}_{crit.}))$.¹ This happens however at the cost of re-tuning HICIS and, hence, also AE, that in the case of small-amplitude perturbations of $N(\mathbf{p}_{crit.}, l_\alpha(\mathbf{p}_{crit.}))$, are expected to be up- and down-regulated toward and away from the critical point, respectively, in a power-law fashion described by r2 (Fig. 5c). Mutation-induced perturbations propagating throughout the structure are thus expected to be amplified in the vicinity of the critical point while, on the other hand, to be damped out toward the interior (i.e., toward the HP and the SF) and toward channel exterior bounded by outer pore surface radius. Given that mutations occurring in the structural proximity of the SF are highly likely to have a deleterious LOF effect [94], observed damping-out mechanism might act as a shield protecting SF's biological machinery from mutations occurring within the pre-inflection phase. On the other hand, mutations occurring in the post-inflection phase are unlikely to perturb the SF as they have to overcome a large energy barrier in order to reach channel interior. We thus hypothesize that critical clustering of pain-related mutation sites might actually reflect a trade-off between the two extremes; a destructive destabilization and an insignificant one.

We tested the critical-clustering hypothesis by calculating the distance of each mutation site from SF's critical point (Additional file 1: S9b) and feeding retrieved distances into a binary classifier. We achieved to classify correctly 28 (out of 36) and 39 (out of 48) of pain-related and neutral mutation sites correctly with a cut-off distance of $\sim 5.8 \text{ \AA}$. This translates to an area under receiver operating characteristics (ROC) curve of 0.824 and pain phenotype prediction with specificity of 0.812 and sensitivity of 0.777 (Fig. 6a). Intuitive geometrical depiction of this result requires to think of a

¹ The average number of atoms per amino acid is 19.2 corresponding to a minor fraction of $N_c = 18567$ atoms composing the NaV1.7 structural model in use. Hence, a missense *SCN9A*-gene mutation resulting in the substitution or deletion of a single amino acid is expected to induce a perturbation of the form $N(\mathbf{p}_{crit.}, l_\alpha(\mathbf{p}_{crit.})) \rightarrow N(\mathbf{p}_{crit.}, l_\alpha(\mathbf{p}_{crit.})) + \epsilon(\mathbf{p}_{crit.}, l_\alpha(\mathbf{p}_{crit.}))$, with $\epsilon(\mathbf{p}_{crit.}, l_\alpha(\mathbf{p}_{crit.}))$ being a small-amplitude perturbation source describing addition and/or removal of a minor number of atoms across different channel scales. Then, HICIS is regulated according to $h_z^{(1)}(\mathbf{p}_{crit.}, l_\alpha(\mathbf{p}_{crit.})) + \zeta(\mathbf{p}_{crit.}, l_\alpha(\mathbf{p}_{crit.})) \sim l_\alpha(\mathbf{p}_{crit.})^{\gamma(\mathbf{p}_{crit.})} \cdot (N(\mathbf{p}_{crit.}, l_\alpha(\mathbf{p}_{crit.})) + \epsilon(\mathbf{p}_{crit.}, l_\alpha(\mathbf{p}_{crit.})))$ with $\gamma(\mathbf{p}_{crit.}) = \gamma_{partI}(\mathbf{p}_{crit.})$ for $s(\mathbf{p}_{crit.}) < l_\alpha(\mathbf{p}_{crit.}) \leq \xi(\mathbf{p}_{crit.})$ and $\gamma(\mathbf{p}_{crit.}) = \gamma_{partII}(\mathbf{p}_{crit.})$ for $\xi(\mathbf{p}_{crit.}) < l_\alpha(\mathbf{p}_{crit.}) \leq o(\mathbf{p}_{crit.})$ so that HII axial field component described by r1 remains intact around the critical point.



“hot” spherical shell squeezed between the spheres of radii $\sim \xi(\mathbf{p}_{crit.}) + 5.8$ Å and $\sim \xi(\mathbf{p}_{crit.}) - 5.8$ Å centered at $\mathbf{p}_{crit.}$ incorporating areas “a1” and “a2” thus containing the majority of pain-related mutation sites. This tendency can be deduced from Fig. 5 where we can see that correctly-classified pain-related and neutral mutation sites tend to minimize and maximize, respectively, their distance from the critical radius $\xi(\mathbf{p}_{crit.})$. The opposite holds for misclassified mutation sites. Note however that due to the pore points offset, distances of sites from $\xi(\mathbf{p}_{crit.})$ line on Fig. 5 are not equal with the distances of their structural locations from the surface of the sphere of $\xi(\mathbf{p})$ (discrepancies are of order 3.13 ± 4.63 Å). Misclassified pain-related mutations are I136V,



W1538R, I1461T, R185H, I228M, I720K, I739V and T1596I indicating that sensitivity output is qualitatively similar to the HP-based classification attempt. On the other hand, quality of specificity differs significantly among classification attempts as critical-point distance criterion misclassified neutrals M145L, M146S, R1207K, T1210N, V1613I, D890N, K1412I, K1415I and S1419N are clustering within the “hot” spherical shell in proximity to HP’s boundary.

Finally, in order to harvest the classification power of both predictors, we linearly combined distance metrics by calculating a weighted distance average (Additional file 1: S11). The weighted distance average achieved to classify correctly 29 (out of 36) pain-related mutations and 45 (out of 48) neutrals, i.e., sensitivity = 0.805, specificity = 0.937,

area under ROC curve = 0.872 (Fig. 7a). The threshold weighted distance value is ~ 9.6 Å and it indicates which mutation sites are found in proximity to SF's critical point and HP's boundary.

The relatively-low sensitivity of the weighted distance average is not surprising if we consider that both classifications attempts failed in correctly classifying pain-related mutation sites found far away from the HP and from the SF; misclassified pain-related mutation sites are I136V, W1538R, I1461T, R185H, I720K, I739V and T1596I and all of them are found within the post-inflection phase with the exception of I1461T which is located within the lag domain but still far away from the HP and from the SF (Figs. 3, 5a and 7). On the other hand, misclassified neutrals R1207K, V1613I and S1419N occupy "hot" spots located in proximity to SF's critical point and HP's boundary (Figs. 3, 5a and 7).

Discussion and concluding remarks

Criticality hypothesis in biology aims at explaining how emergence of power-laws increases biological system's robustness and efficiency hand-in-hand with evolution. Empirical evidence for complex biological systems operating near critical points include cases of gene expression [95], DNA sequences [96], protein structures [63–66], cell growth [97] and neuronal dynamics underlying brain activity [98]. In practice, criticality implies that system dynamics are delicately balanced between an ordered state where perturbations are damped-out and a disordered state where perturbations are amplified. Consequences of critical dynamics are associated with optimal information processing [99], enhanced network stability [100] and maximal sensitivity to external stimuli [101].

In this work, instead of trying to predict the effect of missense *SCN9A*-gene mutations via comparing mutant NaV1.7 structures in silico, we extracted hydrophobic features of the wild-type atomic environment encoding NaV1.7's response to mutation-induced variations. Stated differently, we hypothesized that some regions of the atomic environment around NaV1.7's pore exhibit higher sensitivity to mutation-induced perturbations due to the long-range nature of HIs guaranteeing their stability; a hallmark of SOC is that avalanche-like perturbing effects are amplified and fast-spreading throughout critical network locations [102]. To test this hypothesis we mapped mutation structural locations on their corresponding mutation sites and probed topological and scaling hydrophobic characteristics of the atomic bulk around the pore. Importantly, this is possible due to the relatively-large number of pain-related mutations providing with the opportunity of structure-based mutation statistics and, consequently, identification of densely-populated (by mutation sites) structural domains.

We employed a closed-state structural model of the NaV1.7 that is constructed in silico via homology modeling procedures based on the pre-open NaVAb template (see "Methods" section). By doing so, we sought to initiate our investigations from a well-studied and precisely-engineered protonated NaV1.7 structure that has previously provided with clinically-relevant observations. The fact that the structural model in-use represents a protonated state of the NaV1.7 molecule is crucial here as cumulative hydrophobicity-property moments calculations take explicitly into account hydrogen atoms. Biophysical significance of the structural model in-use was first experimentally validated in [7] where structure-based analysis successfully predicted that the IEM-related V400M and

S241T mutations are energetically coupled and, hence, both exhibiting pharmacoresponsiveness to carbamazepine. The same structural model has later also been used in [30, 58] in order to explain mutation-induced electrophysiological alternations in relation to atomic-level NaV1.7 structural changes. The main structural difference between the model in use here and the 6J8J NaV1.7 [82] structure is that the latter contains the complete DIII-DIV intracellular linker which is a hotspot for PEPD mutations. Thus working with the 6J8J NaV1.7 structure will allow to investigate two more mutation cases, namely, the PEPD-related mutations F1462V [103] and T1464I [15]. Given however that the present scheme fails in classifying correctly the PEPD-related I1461T mutation, it is rather unlikely that it will succeed with F1462V or T1464I. The reason for this misclassification is that the IS end of the channel, where the DIII-DIV linker helix is found, is predominantly hydrophilic and far away from the SF (see Figs. 3 and 5a).

The starting point of the presented procedures was the approximation of the atomic cumulative distribution function around NaV1.7's pore demonstrating that packing of atoms follows a sigmoid pattern. The generality of the Richards model was found to be adequate for this modeling purpose verifying the sigmoid CDF hypothesis and, consequently, revealing a biphasic spatial organization of the atomic environment around the pore dictated by the spatial transition from the PM from the VSs. We showed that the pore is lined by a HP dominating within channel interior and that HIs stabilizing atom-packing around the SF are critically tuned with respect to the local inflection points. This NaV1.7 feature is shared with its evolutionary-ancestor, namely, with the pre-open NaVAb channel, suggesting that location and nature of HIs critical tuning might be conserved from NaVChs of bacterial homomers to NaVChs of mammalian heteromers [69].

Pain-related mutations tend to occupy structural locations in proximity to HP's boundary while maintaining a critical HIs-distance from the SF. Geometrically, this result indicates that the majority of pain-related mutations are found within a spherical shell around the SF incorporating parts of the HP. What might be the evolutionary principle underlying this non-random mutation distribution around NaV1.7's pore? Given that the hydrophilic DEKA SF sequence is conserved among human and non-human NaVCh templates [82], we propose that occurrence of mutations at critical hydrophobic-interactions distance from the SF might reflect an evolutionary trade-off between potentially-deleterious destabilizations occurring too close to the SF, and insignificant polymorphisms occurring far away from it. According to this rationale, mutations occupying critical hydrophobic-interactions network locations lead to a GOF effect by increasing channel's configurational space and, consequently, expanding physiological range of ion currents, while not risking structure deletion or severe destabilizations that can induce a LOF effect [94].

Misclassification of seven pain-related events found within the post-inflection phase (namely, of I136V, W1538R, I1461T, R185H, I720K, I739V and T1596I) suggests that the destabilizing mutation effect within the post-inflection phase and, specifically, within the VSs needs to be locally investigated. In particular, misclassified pain-related events are likely to perturb local features of the VSs which are however crucial for physiological gating behavior. It might therefore be useful for future studies to consider a decoupling of the PM from the VSs in order to focus solely on the cumulative hydrophobic topology and HIs-networking within the VSs. Alternatively, considering biophysical

characteristics of substituted amino acids (e.g., size, charge, degree of conservation) might also contribute in improving classification accuracy as it would provide a more detailed picture of the mutation effect.

Admittedly, a limitation of this study is the small (from a statistics point of view) number of available mutation sites. To resolve this issue and provide with stronger statistical validation, we may consider in future studies to increase number of neutral and pain-related mutations, for example, by introducing NaV1.7 variants found in the Genome Aggregation Database (gnomAD) [104]. A methodological weakness is that we neglected radial hydrophobic effects. In particular, even if the amplitude of the HIIS radial field component is decreasing (in comparison to the amplitude of the HIIS axial field component) for increasing molecular scale, its contribution cannot be neglected for interactions between penetrating ions species and pore walls.

In summary, our findings suggest that pathophysiological evaluation of mutation sites with respect to cumulative NaV1.7 hydrophobic properties can be performed with negligible computational effort and similar or even higher accuracy to [59] (reported accuracy: 0.81) but also to the more recent study of [61] where a MLE computational pipeline was employed (reported accuracy on the human NaV1.7 template: 63.5%). Given that the formation of a narrow and hydrophilic SF followed by a wide and hydrophobic CC is a widely conserved pore-architectural motif, our observations might be relevant for other voltage-gated channel species as well. Crucially, hydrophobicity-property has been previously recognized as a key-marker for predicting functional outcome of genetic defects not only in NaVChs, but also in voltage-gated calcium [94] and potassium channels [105]. Finally, in an era where MLE pipelines become increasingly popular, the phenomenological framework curated in this study could provide a phenomenological basis for biophysical interpretation of MLE-retrieved predictions regarding NaVChs pathophysiological characterization and help in tracing them back on the atomic structure in a site-specific manner as recently attempted in [106].

Supplementary Information

The online version contains supplementary material available at <https://doi.org/10.1186/s12859-021-04119-2>.

Additional file 1: Supplementary information.

Acknowledgements

We acknowledge technical and scientific support provided by the PROPANE study group.

Authors' contributions

MNX designed the study, performed computations, and analyzed the data; DK, RW and PL contributed to refinement of algorithmic procedures; YY provided with the 3D structural model of the NaV1.7 channel; MMG contributed to variants selection and classification; RW, PL, DK, YY, JH, HJS and SGW provided with critical feedback and helped with the interpretation of the results; YY and SGW encouraged MNX to focus on specific aspects of the findings; HJS supervised the study; GL and CGF were in charge of overall direction; MNX wrote the manuscript in consultation with all the co-authors; All co-authors have critically revised the manuscript. All authors read and approved the final manuscript.

Funding

The study was partly funded by the European Union 7th Framework Programme (Grant n602273).

Availability of data and materials

Data sharing is not applicable to this article as no datasets were generated or analyzed during the current study. The 3D structural model of the NaV1.7 channel is available from the authors with permission of YY and SGW.

Declarations

Ethics approval and consent to participate

Not applicable.

Competing interests

The authors declare that they have no competing interests.

Author details

¹Department of Toxicogenomics, Section Clinical Genomics, Maastricht University, PO Box 616, 6200 MD Maastricht, The Netherlands. ²Research School for Mental Health and Neuroscience (MHeNS), Maastricht University, PO Box 616, 6200 MD Maastricht, The Netherlands. ³Neuroalgology Unit, Fondazione IRCCS Istituto Neurologico “Carlo Besta”, Via Celoria 11, 20133 Milan, Italy. ⁴Department of Medicinal Chemistry and Molecular Pharmacology, Purdue University College of Pharmacy, West Lafayette, IN 47907, USA. ⁵Purdue Institute for Integrative Neuroscience, West Lafayette, IN 47907, USA. ⁶Department of Clinical Genetics, Maastricht University Medical Center, PO box 5800, 6202 AZ Maastricht, The Netherlands. ⁷Department of Cardiology, CARIM School for Cardiovascular Diseases, Maastricht University, PO Box 616, 6200 MD Maastricht, The Netherlands. ⁸Department of Neurology and Center for Neuroscience and Regeneration Research, Yale University School of Medicine, New Haven, CT 06510, USA. ⁹Rehabilitation Research Center, Veterans Affairs Connecticut Healthcare System, West Haven, CT 06516, USA. ¹⁰Department of Biomedical and Clinical Sciences “Luigi Sacco”, University of Milan, Via G.B. Grassi 74, 20157 Milan, Italy. ¹¹Department of Neurology, Maastricht University Medical Center, PO Box 5800, 6202 AZ Maastricht, The Netherlands. ¹²Department of Data Science and Knowledge Engineering, Maastricht University, PO Box 616, 6200 MD Maastricht, The Netherlands. ¹³Research School for Oncology and Developmental Biology (GROW), Maastricht University, PO Box 616, 6200 MD Maastricht, The Netherlands.

Received: 18 December 2020 Accepted: 1 April 2021

Published online: 23 April 2021

References

- Cheng X, Dib-Hajj SD, Tyrrell L, Waxman SG. Mutation I136V alters electrophysiological properties of the Na(v)1.7 channel in a family with onset of erythromelalgia in the second decade. *Mol Pain*. 2008;4:1.
- Estacion M, Choi JS, Eastman EM, et al. Can robots patch-clamp as well as humans? Characterization of a novel sodium channel mutation. *J Physiol*. 2010;588:1915–27.
- Wu MT, Huang PY, Yen CT, Chen CC, Lee MJ. A novel SCN9A mutation responsible for primary erythromelalgia and is resistant to the treatment of sodium channel blockers. *PLoS ONE*. 2013;8:e55212.
- Choi JS, Dib-Hajj SD, Waxman SG. Inherited erythromelalgia: limb pain from an S4 charge-neutral Na channelopathy. *Neurology*. 2006;67:1563–7.
- Ahn HS, Dib-Hajj SD, Cox JJ, et al. A new Nav1.7 sodium channel mutation I234T in a child with severe pain. *Eur J Pain*. 2010;14:944–50.
- Lampert A, Dib-Hajj SD, Tyrrell L, Waxman SG. Size matters: erythromelalgia mutation S241T in Nav1.7 alters channel gating. *J Biol Chem*. 2006;281:36029–35.
- Yang Y, Dib-Hajj SD, Zhang J, Zhang Y, Tyrrell L, Estacion M, Waxman SG. Structural modeling and mutant cycle analysis predict pharmacoresponsiveness of a Nav1.7 mutant channel. *Nat Commun*. 2012;3:1186.
- Emery EC, Habib AM, Cox JJ, et al. Novel SCN9A mutations underlying extreme pain phenotypes: unexpected electrophysiological and clinical phenotype correlations. *J Neurosci*. 2015;35:7674–81.
- Sheets PL, Jackson JO 2nd, Waxman SG, Dib-Hajj SD, Cummins TR. A Nav1.7 channel mutation associated with hereditary erythromelalgia contributes to neuronal hyperexcitability and displays reduced lidocaine sensitivity. *J Physiol*. 2007;581:1019–31.
- Fischer TZ, Gilmore ES, Estacion M, et al. A novel Nav1.7 mutation producing carbamazepine-responsive erythromelalgia. *Ann Neurol*. 2009;65:733–41.
- Lampert A, Dib-Hajj SD, Eastman EM, Tyrrell L, Lin Z, Yang Y, Waxman SG. Erythromelalgia mutation L823R shifts activation and inactivation of threshold sodium channel Nav1.7 to hyperpolarized potentials. *Biochem Biophys Res Commun*. 2006;390:319–24.
- Wu B, Zhang Y, Tang H, et al. A novel SCN9A mutation (F826Y) in primary erythromelalgia alters the excitability of Nav1.7. *Curr Mol Med*. 2017;17:450–7.
- Cummins TR, Dib-Hajj SD, Waxman SG. Electrophysiological properties of mutant Nav1.7 sodium channels in a painful inherited neuropathy. *J Neurosci*. 2004;24:8232–6.
- Han C, Dib-Hajj SD, Lin Z, et al. Early- and late-onset inherited erythromelalgia: genotype–phenotype correlation. *Brain*. 2009;132:1711–22.
- Theile JW, Cummins TR. Inhibition of Navβ4 peptide-mediated resurgent sodium currents in Nav1.7 channels by carbamazepine, riluzole, and anandamide. *Mol Pharmacol*. 2011;80:724–34.
- Tanaka BS, Nguyen PT, Zhou EY, et al. Gain-of-function mutation of a voltage-gated sodium channel Nav1.7 associated with peripheral pain and impaired limb development. *J Biol Chem*. 2017;292:9262–72.
- Hoeijmakers JG, Han C, Merkies IS, et al. Small nerve fibres, small hands and small feet: a new syndrome of pain, dysautonomia and acromesomelia in a kindred with a novel Nav1.7 mutation. *Brain*. 2012;135:345–58.
- Cummins TR, Dib-Hajj SD, Waxman SG. Electrophysiological properties of mutant Nav1.7 sodium channels in a painful inherited neuropathy. *J Neurosci*. 2004;24:8232–6.
- Rush AM, Dib-Hajj SD, Liu S, Cummins TR, Black JA, Waxman SG. A single sodium channel mutation produces hyper- or hypoexcitability in different types of neurons. *Proc Natl Acad Sci USA*. 2006;103:8245–50.

20. Han C, Rush AM, Dib-Hajj SD, et al. Sporadic onset of erythromelgia: a gain-of-function mutation in Nav1.7. *Ann Neurol*. 2006;59:553–8.
21. Harty TP, Dib-Hajj SD, Tyrrell L, Blackman R, Hisama FM, Rose JB, Waxman SG. Na_v1.7 mutant A863P in erythromelgia: effects of altered activation and steady-state inactivation on excitability of nociceptive dorsal root ganglion neurons. *J Neurosci*. 2006;26:12566–75.
22. Choi JS, Zhang L, Dib-Hajj SD, et al. Mexiletine-responsive erythromelgia due to a new Na(v)1.7 mutation showing use-dependent current fall-off. *Exp Neurol*. 2009;216:383–9.
23. Stadler T, O'Reilly AO, Lampert A. Erythromelgia mutation Q875E Stabilizes the activated state of sodium channel Nav1.7. *J Biol Chem*. 2015;290:6316–25.
24. Cheng X, Dib-Hajj SD, Tyrrell L, Te Morsche RH, Drenth JP, Waxman SG. Deletion mutation of sodium channel Na(V)1.7 in inherited erythromelgia: enhanced slow inactivation modulates dorsal root ganglion neuron hyperexcitability. *Brain*. 2011;134:1972–86.
25. Cheng X, Dib-Hajj SD, Tyrrell L, Wright DA, Fischer TZ, Waxman SG. Mutations at opposite ends of the DIII/S4-S5 linker of sodium channel Nav1.7 produce distinct pain disorders. *Mol Pain*. 2010;6:24.
26. Estacion M, Yang Y, Dib-Hajj SD, et al. A new Nav1.7 mutation in an erythromelgia patient. *Biochem Biophys Res Commun*. 2013;432:99–104.
27. Dib-Hajj SD, Rush AM, Cummins TR, et al. Gain-of-function mutation in Nav1.7 in familial erythromelgia induces bursting of sensory neurons. *Brain*. 2005;128:1847–54.
28. Cregg R, Laguda B, Werdehausen R, et al. Novel mutations mapping to the fourth sodium channel domain of Nav1.7 result in variable clinical manifestations of primary erythromelgia. *Neuromol Med*. 2013;15:265–78.
29. Eberhardt M, Nakajima J, Klinger AB, et al. Inherited pain: sodium channel Nav1.7 A1632T mutation causes erythromelgia due to a shift of fast inactivation. *J Biol Chem*. 2014;289:1971–80.
30. Yang Y, Huang J, Mis MA, et al. Nav1.7-A1632G mutation from a family with inherited erythromelgia: enhanced firing of dorsal root ganglia neurons evoked by thermal stimuli. *J Neurosci*. 2016;36:7511–22.
31. Jarecki BW, Sheets PL, Jackson JO 2nd, Cummins TR. Paroxysmal extreme pain disorder mutations within the D3/S4-S5 linker of Nav1.7 cause moderate destabilization of fast inactivation. *J Physiol*. 2008;586:4137–53.
32. Theile JW, Jarecki BW, Piekarczyk AD, Cummins TR. Nav1.7 mutations associated with paroxysmal extreme pain disorder, but not erythromelgia, enhance Navβ4 peptide-mediated resurgent sodium currents. *J Physiol*. 2011;589:597–608.
33. Furtleman CR, Baker MD, Parker KA, et al. SCN9A mutations in paroxysmal extreme pain disorder: allelic variants underlie distinct channel defects and phenotypes. *Neuron*. 2006;52:767–74.
34. Choi JS, Boralevi F, Brissaud O, et al. Paroxysmal extreme pain disorder: a molecular lesion of peripheral neurons. *Nat Rev Neurol*. 2011;7:51–5.
35. Suter MR, Bhuiyan ZA, Laedermann CJ, et al. p.L1612P, a novel voltage-gated sodium channel Nav1.7 mutation inducing a cold sensitive paroxysmal extreme pain disorder. *Anesthesiology*. 2015;122:414–23.
36. Dib-Hajj SD, Estacion M, Jarecki BW, et al. Paroxysmal extreme pain disorder M1627K mutation in human Nav1.7 renders DRG neurons hyperexcitable. *Mol Pain*. 2008;4:37.
37. Estacion M, Dib-Hajj SD, Benke PJ, et al. NaV1.7 gain-of-function mutations as a continuum: A1632E displays physiological changes associated with erythromelgia and paroxysmal extreme pain disorder mutations and produces symptoms of both disorders. *J Neurosci*. 2008;28:1079–11088.
38. Han C, Hoeijmakers JG, Liu S, et al. Functional profiles of SCN9A variants in dorsal root ganglion neurons and superior cervical ganglion neurons correlate with autonomic symptoms in small fibre neuropathy. *Brain*. 2012;135:2613–28.
39. Estacion M, Han C, Choi JS, et al. Intra- and interfamily phenotypic diversity in pain syndromes associated with a gain-of-function variant of NaV1.7. *Mol Pain*. 2011;7:92.
40. Faber CG, Hoeijmakers JG, Ahn HS, et al. Gain of function Nav1.7 mutations in idiopathic small fiber neuropathy. *Ann Neurol*. 2012;71:26–39.
41. Huang J, Yang Y, Dib-Hajj SD, et al. Depolarized inactivation overcomes impaired activation to produce DRG neuron hyperexcitability in a Nav1.7 mutation in a patient with distal limb pain. *J Neurosci*. 2014;34:12328–40.
42. Blesneac I, Themistocleous AC, Fratter C, et al. Rare NaV1.7 variants associated with painful diabetic peripheral neuropathy. *Pain*. 2018;159:469–80.
43. Cox JJ, Reimann F, Nicholas AK, et al. An SCN9A channelopathy causes congenital inability to experience pain. *Nature*. 2006;444:894–8.
44. Goldberg YP, MacFarlane J, MacDonald ML, et al. Loss-of-function mutations in the NaV1.7 gene underlie congenital indifference to pain in multiple human populations. *Clin Genet*. 2007;71:311–9.
45. Nilsen KB, Nicholas AK, Woods CG, Mellgren SI, Nebuchennykh M, Aasly J. Two novel SCN9A mutations causing insensitivity to pain. *Pain*. 2009;143:155–8.
46. Hammer MU, Anderson TH, Chaimovich A, Shell MS, Israelachvili J. The search for the hydrophobic force law. *Faraday Discuss*. 2010;146:299–308.
47. Hummer G, Garde S, García AE, Paulaitis ME, Pratt LR. Hydrophobic effects on a molecular scale. *J Phys Chem B*. 1998;102:51.
48. Aryal P, Sansom MSP, Tucker SJ. Hydrophobic gating in ion channels. *J Mol Biol*. 2015;427:121–30.
49. Yonkunas M, Kurnikova M. The hydrophobic effect contributes to the closed state of a simplified ion channel through a conserved hydrophobic patch at the pore-helix crossing. *Front Pharmacol*. 2015;6:284.
50. Li E, Wimley WC, Hristova K. Transmembrane helix dimerization: beyond the search for sequence motifs. *Biochim Biophys Acta*. 2012;1818:183–93.
51. Lin J, Motylinski J, Krauson AJ, Wimley WC, Searson PC, Hristova K. Interactions of membrane active peptides with planar supported bilayers: an impedance spectroscopy study. *Langmuir*. 2012;28:6088–96.
52. Yu FH, Catterall WA. The VGL-chnome: a protein superfamily specialized for electrical signaling and ionic homeostasis. *Sci STKE*. 2004;253:re15.

53. Chugunov AO, Volynsky PE, Krylov NA, Nolde DE, Efremov RG. Temperature-sensitive gating of TRPV1 channel as probed by atomistic simulations of its trans- and juxtamembrane domains. *Sci Rep*. 2016;6:33112.
54. Chen X, Yan J, Aldrich RW. BK channel opening involves side-chain reorientation of multiple deep-pore residues. *Proc Natl Acad Sci USA*. 2014;111:E79–88.
55. Saotome K, Teng B, Tsui CC, et al. Structures of the otopetrin proton channels Otop1 and Otop3. *Nat Struct Mol Biol*. 2019;26:518–25.
56. Chamberlin A, Qiu F, Rebolledo S, Wang Y, Noskov SY, Larsson PH. Hydrophobic plug functions as a gate in voltage-gated proton channels. *Proc Natl Acad Sci USA*. 2014;111:E273–82.
57. Lampert A, O'Reilly AO, Dib-Hajj SD, Tyrrell L, Wallace BA, Waxman SG. A pore-blocking hydrophobic motif at the cytoplasmic aperture of the closed-state Nav1.7 channel is disrupted by the erythromelalgia-associated F1449V mutation. *J Biol Chem*. 2008;283:24118–27.
58. Yang Y, Estacion M, Dib-Hajj SD, Waxman SG. Molecular architecture of a sodium channel S6 helix: radial tuning of the voltage-gated sodium channel 1.7 activation gate. *J Biol Chem*. 2013;288:13741–7.
59. Kapetis D, Yang Y, Sassone J, et al. Network topology of Nav1.7 mutations in sodium channel-related painful disorders. *BMC Syst Biol*. 2017;11:28.
60. Hasan S, Hunter T, Hunter G, Pessia M, D'Adamo MC. Commentary: A channelopathy mutation in the voltage-sensor discloses contributions of a conserved phenylalanine to gating properties of Kv1.1 channels and ataxia. *Front Cell Neurosci*. 2018;12:174.
61. Toffano A, Chiarot G, Zamuner S, et al. Computational pipeline to probe Nav1.7 gain-of-functions variants in neuropathic painful syndromes. *Sci Rep*. 2020;10:17930.
62. Bak P, Tang C, Wiesenfeld K. Self-organized criticality: an explanation of 1/f noise. *Phys Rev Lett*. 1987;59:381–4.
63. Phillips JC. Scaling and self-organized criticality in proteins I. *Proc Natl Acad Sci USA*. 2009;106:3107–12.
64. Phillips JC. Scaling and self-organized criticality in proteins II. *Proc Natl Acad Sci USA*. 2009;106:3113–8.
65. Morett M. Self-organized critical model for protein folding. *Physica A*. 2011;390:3055–9.
66. Phillips JC. Self-organized criticality in proteins: hydrophobic roughening profiles of G-protein-coupled receptors. *Phys Rev E*. 2013;87:032709.
67. Zhou R, Silverman BD, Royyuru AK, Athma P. Spatial profiling of protein hydrophobicity: native vs. decoy structures. *Proteins*. 2003;52:561–72.
68. Xenakis MN, Kapetis D, Yang Y, et al. Cumulative hydrophobic topology of a voltage-gated sodium channel at atomic resolution. *Proteins*. 2020;88:1319–28.
69. Xenakis MN, Kapetis D, Yang Y, et al. Non-extensivity and criticality of atomic hydrophobicity around a voltage-gated sodium channel's pore; a modeling study. *J Biol Phys*. 2021;47(1):61–77.
70. Jan LY, Jan YN. A superfamily of ion channels. *Nature*. 1990;345:672.
71. Keynes RD, Elinder F. The screw-helical voltage gating of ion channels. *Proc Biol Sci*. 1999;266:843–52.
72. Tikhonov DB, Zhorov BS. Possible roles of exceptionally conserved residues around the selectivity filters of sodium and calcium channels. *J Biol Chem*. 2011;286:2998–3006.
73. R Core Team. R: a language and environment for statistical computing. R Foundation for Statistical Computing, Vienna, Austria. <http://www.R-project.org/> (2014).
74. Payandeh J, Scheuer T, Zheng N, Catterall WA. The crystal structure of a voltage-gated sodium channel. *Nature*. 2011;475:353–8.
75. Zhang J, Zhang Y. GPCRDB: G protein-coupled receptor spatial restraint database for 3D structure modeling and function annotation. *Bioinformatics*. 2010;26:3004–5.
76. Zhang J, Liang Y, Zhang Y. Atomic-level protein structure refinement using fragment-guided molecular dynamics conformation sampling. *Structure*. 2011;19:1784–95.
77. Zhang J, Zhang Y. A novel side-chain orientation dependent potential derived from random-walk reference state for protein fold selection and structure prediction. *PLoS ONE*. 2010;5:e15386.
78. Zhang Y, Skolnick J. TM-align: a protein structure alignment algorithm based on the TM-score. *Nucleic Acids Res*. 2005;33:2302–9.
79. Dudley SC Jr, Chang N, Hall J, Lipkind G, Fozzard HA, French RJ. μ -conotoxin GIIIA interactions with the voltage-gated Na⁺ channel predict a clockwise arrangement of the domains. *J Gen Physiol*. 2000;116:679–90.
80. Li RA, Ennis IL, French RJ, Dudley SC Jr, Tomaselli GF, Marbàn E. Clockwise domain arrangement of the sodium channel revealed by μ -conotoxin (GIIIA) docking orientation. *J Biol Chem*. 2001;276:11072–7.
81. Zhang J, Zhang Y. A novel side-chain orientation dependent potential derived from random-walk reference state for protein fold selection and structure prediction. *PLoS ONE*. 2010;5:e15386.
82. Shen H, Liu D, Wu K, Lei J, Yan N. Structures of human Nav1.7 channel in complex with auxiliary subunits and animal toxins. *Science*. 2019;363:1303–8.
83. Humphrey W, Dalke A, Schulten K. VMD-visual molecular dynamics. *J Mol Graph*. 1996;14:33–8.
84. Kahm M, Hasenbrink G, Lichtenberg-Fraté H, Ludwig J, Kschischo M. Fitting biological growth curves with R. *J Stat Softw*. 2010;33:1–21.
85. Zwietering MH, Jongenburger I, Rombouts FM, van't Riet K. Modeling of the bacterial growth curve. *Appl Environ Microbiol*. 1990;56:1875–81.
86. Blumberg AA. Logistic growth rate functions. *J Theor Biol*. 1968;21:42.
87. Gompertz B. On the nature of the function expressive of the law of human mortality, and on a new mode of determining the value of life contingencies. *Philos Trans R Soc Lond*. 1825;115:513–85.
88. Richards FJ. A flexible growth function for empirical use. *J Exp Bot*. 1959;10:290–300.
89. Tjørve E, Tjørve KMC. A unified approach to the Richards-model family for use in growth analyses: why we need only two model forms. *J Theor Biol*. 2010;267:417–25.
90. Eisenberg D, Weiss RM, Terwilliger TC, Wilcox W. Hydrophobic moments and protein structure. *Faraday Symp Chem Soc*. 1982;17:109–20.
91. Kapcha LH, Rossky PJ. A simple atomic-level hydrophobicity scale reveals protein interfacial structure. *J Mol Biol*. 2014;426:484–98.

92. Wallis Y, Payne S, McAnulty C et al. Practice guidelines for the evaluation of pathogenicity and reporting of sequence variants in clinical molecular genetics. ACGS (2013). http://www.acgs.uk.com/media/774853/evaluation_and_reporting_of_sequence_variants_bpgs_june_2013_-_finalpdf.pdf. Accessed May 25 2013.
93. Robin X, Turck N, Hainard A, Tiberti N, Lisacek F, Sanchez J, Müller M. pROC: an open-source package for R and S+ to analyze and compare ROC curves. *BMC Bioinform*. 2011;12:77.
94. Heyne HO, Baez-Nieto D, Iqba S, et al. A machine learning method can predict loss- versus gain-of-function effects of human genetic variants in disease-associated ion channels. *Sci Transl Med*. 2020;12:556.
95. Tsuchiya M, Giuliani A, Hashimoto M, Erenpreisa J, Yoshikawa K. Self-organizing global gene expression regulated through criticality: mechanism of the cell-fate change. *PLoS ONE*. 2016;11:12.
96. Pavlos GP, Karakatsanis LP, Iliopoulos AC, et al. Measuring complexity, nonextensivity and chaos in the DNA sequence of the major histocompatibility complex. *Physica A*. 2015;438:188–209.
97. Furusawa C, Kaneko K. Adaptation to optimal cell growth through self-organized criticality. *Phys Rev Lett*. 2012;108:208103.
98. Janina H, Gross T. Self-organized criticality as a fundamental property of neural systems. *Front Syst Neurosci*. 2014;8:166.
99. Beggs JM. The criticality hypothesis: how local cortical networks might optimize information processing. *Phil Trans R Soc A*. 2008;366:329–43.
100. Bertschinger N, Natschläger T. Real-time computation at the edge of chaos in recurrent neural networks. *Neural Comput*. 2004;16:1413–36.
101. Kinouchi O, Copelli M. Optimal dynamical range of excitable networks at criticality. *Nat Phys*. 2006;2:348–51.
102. Watkins NW, Pruessner G, Chapman SC, et al. 25 years of self-organized criticality: concepts and controversies. *Space Sci Rev*. 2016;198:3–44.
103. Fertleman CR, Baker MD, Parker KA, Moffatt S, et al. SCN9A mutations in paroxysmal extreme pain disorder: allelic variants underlie distinct channel defects and phenotypes. *Neuron*. 2006;52:767–74.
104. Karczewski KJ, Francioli LC, Tiao G et al. Variation across 141,456 human exomes and genomes reveals the spectrum of loss-of-function intolerance across human protein-coding genes. *bioRxiv*. 2019;531210
105. Stead LF, Wood IC, Westhead DR. KvSNP: accurately predicting the effect of genetic variants in voltage-gated potassium channels. *Bioinformatics*. 2011;27:2181–6.
106. Iqbal S, Pérez-Palma E, Jespersen JB, et al. Comprehensive characterization of amino acid positions in protein structures reveals molecular effect of missense variants. *Proc Natl Acad Sci USA*. 2020;117:28201–11.

Publisher's Note

Springer Nature remains neutral with regard to jurisdictional claims in published maps and institutional affiliations.

Ready to submit your research? Choose BMC and benefit from:

- fast, convenient online submission
- thorough peer review by experienced researchers in your field
- rapid publication on acceptance
- support for research data, including large and complex data types
- gold Open Access which fosters wider collaboration and increased citations
- maximum visibility for your research: over 100M website views per year

At BMC, research is always in progress.

Learn more biomedcentral.com/submissions

